Zemmouri earthquake rupture zone (Mw 6.8, Algeria): Aftershocks sequence relocation and 3D velocity model

A. Ayadi, C. Dorbath, F. Ousadou, S. Maouche, M. Chikh, M. A. Bounif, M. Meghraoui

Zemmouri earthquake rupture zone (M_w 6.8, Algeria): Aftershocks sequence relocation and 3D velocity model

A. Ayadi,[1] C. Dorbath,[2,5] F. Ousadou,[1] S. Maouche,[1] M. Chikh,[3] M. A. Bounif,[4] and M. Meghraoui[5]

Received 4 July 2007; revised 9 April 2008; accepted 18 June 2008; published 4 September 2008.

[1] We analyze the aftershocks sequence of the Zemmouri thrust faulting earthquake (21 May 2003, M_w 6.8) located east of Algiers in the Tell Atlas. The seismic sequence located during ~2 months following the mainshock is made of more than 1500 earthquakes and extends NE–SW along a ~60-km fault rupture zone crossing the coastline. The earthquake relocation was performed using handpicked P and S phases located with the tomoDD in a detailed 3D velocity structure of the epicentral area. Contrasts between velocity patches seem to correlate with contacts between granitic–volcanic basement rocks and the sedimentary formation of the eastern Mitidja basin. The aftershock sequence exhibits at least three seismic clouds and a well-defined SE-dipping main fault geometry that reflects the complex rupture. The distribution of seismic events presents a clear contrast between a dense SW zone and a NE zone with scattered aftershocks. We observe that the mainshock locates between the SW and NE seismic zones; it also lies at the NNS–SSE contact that separates a basement block to the east and sedimentary formations to the west. The aftershock distribution also suggests fault bifurcation at the SW end of the fault rupture, with a 20-km-long ~N 100° trending seismic cluster, with a vertical fault geometry parallel to the coastline juxtaposed. Another aftershock cloud may correspond to 75° SE dipping fault. The fault geometry and related SW branches may illustrate the interference between pre-existing fault structures and the SW rupture propagation. The rupture zone, related kinematics, and velocity contrasts obtained from the aftershocks distribution are in agreement with the coastal uplift and reflect the characteristics of an active zone controlled by convergent movements at a plate boundary.

Citation: Ayadi, A., C. Dorbath, F. Ousadou, S. Maouche, M. Chikh, M. A. Bounif, and M. Meghraoui (2008), Zemmouri earthquake rupture zone (M_w 6.8, Algeria): Aftershocks sequence relocation and 3D velocity model, *J. Geophys. Res.*, *113*, B09301, doi:10.1029/2007JB005257.

1. Introduction

[2] Large and moderate earthquakes are followed by aftershock sequences that may reveal the mainshock rupture zone. Since *Thurber* [1983], several tomographic studies of source areas of strong earthquakes have been performed in various active tectonic domains, demonstrating the contribution of local earthquake tomography to constrain active tectonic structures and the rupture process. Recently, *Zhang and Thurber* [2003] developed a double-difference tomography method, based on hypoDD [*Waldhauser and Ellsworth*, 2000], using absolute and relative P and S-wave travel time data. This improvement allows a better assessment of the 3D crustal velocity model and enhances the seismic event location in comparison to standard local earthquake tomographies. The application of the double-difference seismic tomography (tomoDD) to seismogenic areas has been largely restricted to strike-slip faulting regimes (such as the Hayward fault in California, *Zhang and Thurber* [2003]. Examples of reverse or normal earthquake fault studies using this method include the 2004 (M_w = 6.6) mid-Niigata prefecture earthquake (Japan, *Kato et al.* [2005]) and the 1994 (M_w = 6.7) Arthur's Pass earthquake (New Zealand, *Bannister et al.* [2006]).

[3] The Tell Atlas of northern Algeria is an EW trending thrust and fold belt situated along the Africa-Eurasia plate boundary (Figures 1a and 1b). This active zone generated the 1980 El Asnam thrust fault earthquake (Ms 7.3), which exhibited a complex pattern of thrust and fold structures imaged by a dense aftershocks sequence [*Ouyed et al.*, 1981; *Yielding et al.*, 1989; *Chiarabba et al.*, 1997] (Figure 1a). The Zemmouri earthquake (M_w 6.8) that affected the Tell Atlas in 2003 presents a faulting geometry comparable with the El Asnam seismic event. The seismicity catalogue since AD 1365 makes no mention of the occurrence

[1]Centre de Recherche en Astronomie Astrophysique et Géophysique, Algiers, Algeria.
[2]Institut de Recherche pour le Développement, France.
[3]Centre de Génie Parasismique, Algiers, Algeria.
[4]Université des Sciences et de la Technologie Houari Boumédienne, Algiers, Algeria.
[5]UMR 7516, Institut de Physique du Globe, Strasbourg, France.

0148-0227/08/2007JB005257$09.00

of a large seismic event in the Zemmouri region [*Mokrane et al.*, 1994] and no surface faulting was identified in the earthquake area.

[4] Geodetic measurements (tape, DGPS, and conventional leveling) of the 50-km-long coastal uplift (~0.55 m) lead us to construct a dislocation model with a SE dipping reverse fault mechanism [*Meghraoui et al.*, 2004]. According to the inversion of body waves and the analysis of aftershocks sequence, the Zemmouri event was associated with a SE-dipping, 50–60-km-long reverse fault [*Delouis et al.*, 2004; *Bounif et al.*, 2004]. The rupture propagated bilaterally from the hypocenter. By combining P and S travel-times provided by CRAAG (Centre de Recherche en Astronomie, Astrophysique et Géophysique) National network together with the master events of 27, 28, and 29 May 2003 with M 5.8, M 5.0, and M 5.8 respectively, the main shock was relocated offshore near the coast at 36.85°N, 3.65°E [*Bounif et al.*, 2004]. This coastal epicenter suggests rupture along a previously unidentified offshore fault, which makes constraining the geometry of the fault from geodetic and geologic observations difficult.

[5] During the two months following the main shock, seismic activity was monitored by 25 temporary seismic stations, which recorded a large number (~2500) of aftershocks. Here, we use the aftershocks of the Zemmouri earthquake to illuminate the faulting geometry and velocity structure. We invert absolute and differential times to solve separately for 3D P- and S-wave velocity structure and revised hypocenters using double-difference tomography (tomoDD) [*Zhang and Thurber*, 2003]. We also determine revised focal mechanisms for the aftershock sequence and compute a regional stress tensor.

2. Tectonic Framework

[6] Several disastrous earthquakes, including the 2003 Zemmouri earthquake, have damaged Algiers region and north-central Algeria in the past (2 January 1365, 3 February 1716, 2 March 1825, 2 January 1867, 29 October 1989, 4 September 1996) [*Harbi et al.*, 2004] (Figure 1a). From the stress tensor inversion of CMT focal mechanism solutions, *Stich et al.* [2003] note a dominant NW-SE compression in northern Algeria. Global models of plate movements infer 5–6 mm/year of convergence of Africa toward Eurasia [*Argus et al.*, 1989] of which the Tell Atlas accommodates 2–3 mm/year of shortening along the main thrust system of the plate boundary zone [*Meghraoui and Doumaz*, 1996] (Figure 1a, inset).

[7] The Tell Atlas of northern Algeria is primarily formed by a complex system of thrusts and nappes showing a southern vergence and corresponding to Eocene and early Miocene tectonic episodes [*Wildi*, 1983]. These pre-Neogene units are made of Mesozoic and Cenozoic flyschs units lying for instance on the Blida schists massifs. The overthrusting formations also include metamorphic massifs made of granite, gneiss, and micaschists mainly visible in the Kabylie block near the earthquake area (Figure 1b). Intrusions of volcanic (Calco-Alkalin basaltic formation) units near Cap Djinet suggest the likely existence of active subduction in the Miocene [*Maury et al.*, 2000]. Post-nappe tectonic episodes are responsible for the Neogene and Quaternary basins and show predominant NNW–SSE compression and thrust faulting and folding affecting late Quaternary deposits [*Meghraoui*, 1988].

[8] The Zemmouri earthquake affected the easternmost part of the Neogene and Quaternary Mitidja Basin. The basin contains intensely folded geological units associated with reverse faults and uplifted marine and alluvial terraces [*Meghraoui*, 1988]. The earthquake was also associated with failures of cliffs, rock fall, landslides, and liquefaction in the epicentral zone [*Ayadi et al.*, 2003]. The Mitidja basin is rimmed by prominent EW to ENE–WSW trending late Quaternary faults visible in the Blida fold-and-thrust system to the south, and by the Sahel active fold to the north. The western end of the Mitidja Basin experienced an M_w 6.0 in 29 October 1989, which revealed a complex reverse faulting geometry associated with the Tipaza-Chenoua fold and thrust structure [*Meghraoui*, 1991]. The aftershock study indicated the presence of a NW dipping reverse NE–SW trending fault that extends offshore [*Bounif et al.*, 2003], a scenario comparable with the Zemmouri earthquake but with an antithetic NW dip (Figure 1a). In both cases, the earthquake faults are oblique to the coastline and correlate well with inland active zones. Primary surface fault was not observed during either the 1989 Tipaza or 2003 Zemmouri earthquakes. According to the main shock location, the zone of maximum macroseismic intensity, the coastal uplift, and the SE dipping fault plane of the focal mechanism, it is likely that the 2003 Zemmouri event took place on a fault segment oblique to the coast in continuation of the southern Mitidja basin thrust fault system.

3. Data Collection and Inversion Method

[9] Between 23 May and 31 July 2003, approximately 2500 aftershocks with magnitude Md $\geq$ 1, including three large events with Md $\geq$ 5, were recorded by a temporary network (Figure 2a). The 25 digital seismic stations operated by CRAAG and CGS (Centre de Génie Parasismique) were deployed in the epicentral area, between Algiers and Dellys (Figure 1b). All of them were equipped with short period three-component sensors and synchronized on GPS time. Nine seismic stations were recording continuously with a 75-Hz sampling rate, and all other stations were set on triggered mode. As shown in Figure 2a, this dense network covered the entire area affected by the aftershock sequence, from the coast to 20 km inland.

[10] More than 1000 of the recorded events were located (Figure 2a). The localization has been made using careful manual P and S readings from the temporary network with hypoinverse program [*Klein*, 1978], using the 1D velocity model of *Bezzeghoud et al.* [1994] and *Bounif et al.* [2003]. Reading precision is estimated to be 0.02 to 0.03 s for P-waves and about 0.05 s for S-waves. The magnitudes were calculated using coda length with the coefficients given by *Ouyed* [1981]. The aperture of the seismic array is far from ideal because of the offshore location of about a third of the hypocenters. For tomographic inversion, we use a subset of 929 events with high-quality locations, low rms, and vertical and horizontal uncertainties (rms $\leq$ 0.2, erh $\leq$ 2.5, erz $\leq$ 2.5), and a minimum of 2 S arrivals to better constrain the depth.

[11] The travel-times of the selected aftershocks and the corresponding hypocenter catalogue were used for a

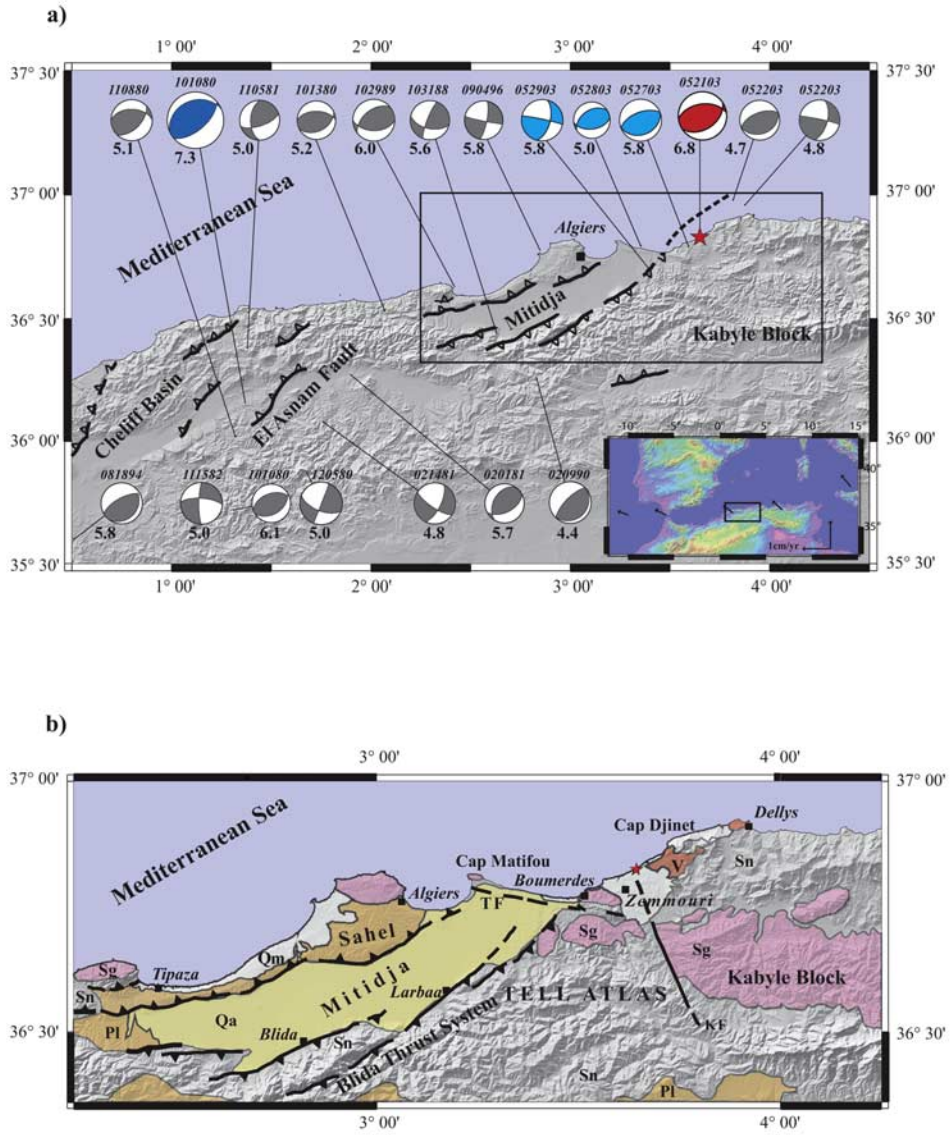

Figure 1. (a) Seimotectonic map of the Tell Atlas of north-central Algeria [*Meghraoui*, 1988] and largest instrumentally recorded events that occurred near Alger [*Harbi et al.*, 2004]. Focal mechanisms are global CMT Harvard solutions; red and light blue solutions are mainshock (red star) and main aftershocks of the Zemmouri earthquake sequence, respectively; dark blue mechanism corresponds to El Asnam major earthquake. The black frame shows the boundaries of Figure 1b. Inset: Location of the study area within the Africa-Eurasia plate boundary and related convergence rate [*Nocquet and Calais*, 2004]. (b) Geology and active tectonics of the North-Central Algeria [*Meghraoui*, 1988]. The red star is the epicentre of the 21 May 2003 Zemmouri earthquake [*Bounif et al.*, 2004]; see also major aftershocks in Figure 2a. Qm: Quaternary marine terraces; Qa: Quaternary alluvial deposits; Pl: Neogene sedimentary units; V: Neogene volcanic fields; Sn: Nappes of flyschs and limestone (Cenozoic and Mesozoic); Sg: Paleozoic granitic basement; lines with black triangles: active thrust fault; simple lines: pre-quaternary fault.

tomographic inversion using the double-difference tomography method developed by *Zhang and Thurber* [2003]. This method uses both the absolute and relative arrival times in a joint solution for hypocentral parameters and P and S wave 3D velocity structure. It improves the accuracy of the velocity structure near the sources and produces earthquake locations with a relative location quality equivalent to that obtained by hypoDD [*Waldhauser and Ellsworth*, 2000]. This improvement is particularly useful for our study, where, because of the offshore location of the fault, the seismic azimuthal gap can exceed 180°.

[12] The double difference (DD) earthquake location algorithm is based on the assumption that if the hypocentral separation between a pair of earthquakes is small compared to the event-station distance and the scale length of the velocity heterogeneity, then the ray paths between the

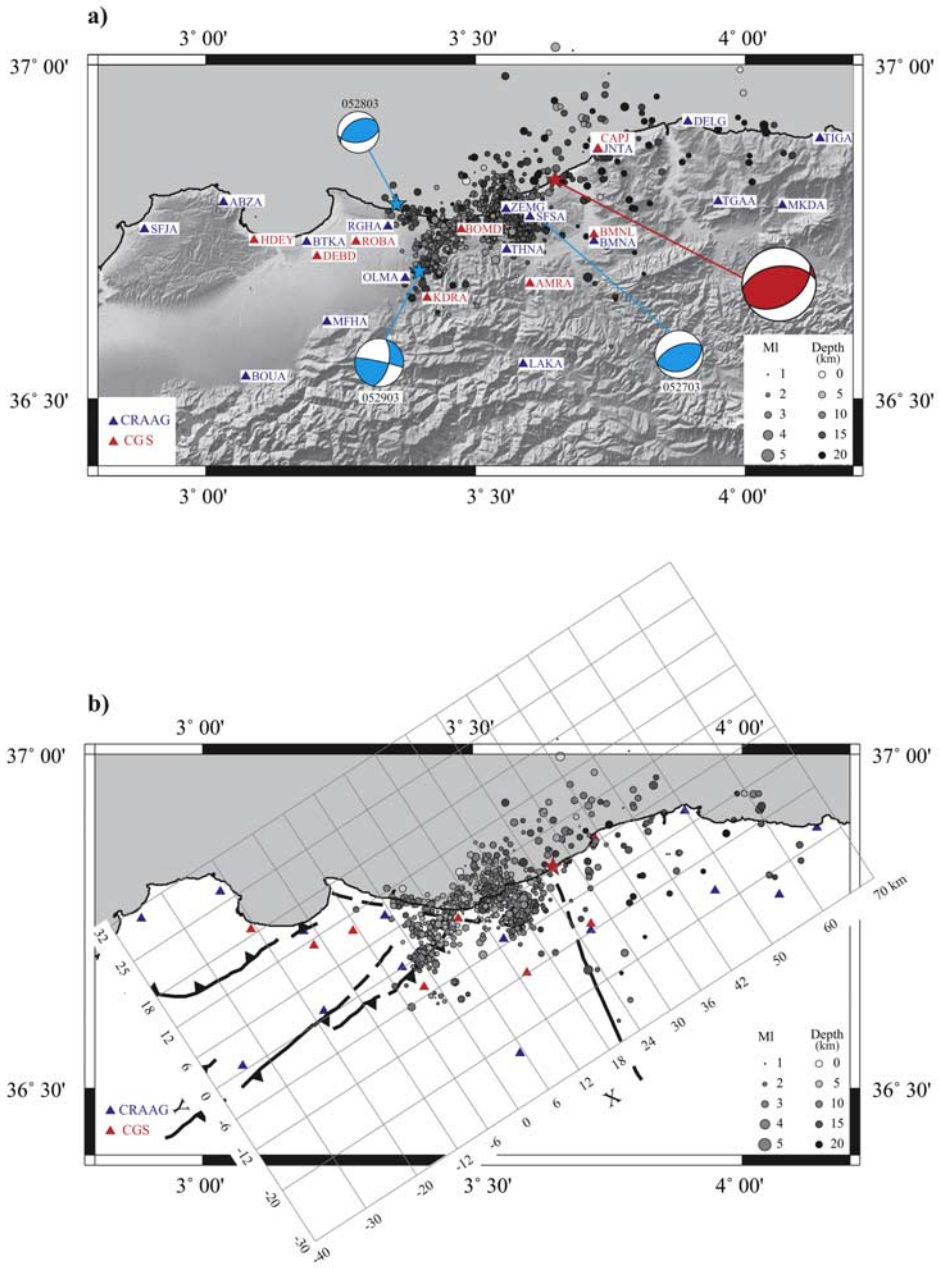

Figure 2. (a) Map view of the aftershocks from 25 May to 31 July, 2003, on a topographic (SRTM) background. The seismic stations used are displayed by triangles, blue for CRAAG, red for CGS. The mainshock location (red star) and 3 largest aftershocks (blue stars) are presented with their focal mechanism. (b) Map view of the relocated aftershocks with the position of the grid nodes used in the tomography study. The rotation is 33° anticlockwise.

source region and a common station are similar along the entire ray path [*Frechet*, 1985; *Got et al.*, 1994]. Thus for closely spaced events, we assume that the path anomalies due to velocity heterogeneity are location-independent. The double difference technique minimizes the residuals between observed and calculated travel time differences for pairs of earthquakes at common stations by iteratively adjusting the vector difference between the hypocenters. However locations of earthquakes far apart may be biased because of velocity heterogeneities. The use of absolute arrival times in the tomoDD method provides valuable information on absolute locations and on broad-scale velocity heterogeneity, while the use of differential times improves the velocity model in the source region relative to standard tomography methods [*Zhang and Thurber*, 2003].

[13] From the 929 selected events, we obtained ~12,200 absolute travel times (~50% each for P and S waves), and from these constructed 238,000 differential travel times for event pairs with inter-event distances of less than 10 km. This distance choice is determined by the 70-km length of the aftershock cloud and the 80-km maximal event-station distance.

[14] The inversion grid chosen after routine tests is presented in Figure 2b. It is rotated 33° anticlockwise, allowing the Y nodes to be almost parallel to the 57°E dipping fault plane. Rotation of the inversion grid does not change the results of the inversion. The distance between the nodes is, from the surface down to the maximal depth of the hypocenters, 6 km, as well as along the X and Y directions in the central part of the grid. After 20 iterations, the weighted rms travel time residual was reduced to 0.05 seconds. The initial P velocity model is interpolated from the 1D models from previous studies [*Ouyed*, 1981; *Bezzeghoud et al.*, 1994; *Bounif et al.*, 2003] and used for the initial hypocentral location. Initial S velocities are directly calculated from P by applying a constant 1.73 Vp/Vs ratio. An inversion of the travel-time data for a 1D velocity model did not provide significant changes to this simple initial model.

[15] Numerous tests have been performed to check the robustness of the 3D solution. We ran tomoDD in LSQR mode and chose a damping at each iteration that results in condition number values between 40 and 50 [*Waldhauser*, 2001]. Several inversions were performed with various strategies of weighting absolute data relatively to differential data. Various distances between the grid nodes were tested in order to get the best trade-off between grid spacing and data resolution. We use the derivative weight sum (DWS) at each node as a measure of the raypath coverage. Thereafter, the iso-value 25, considered to be the limit for resolved structures [*Bannister et al.*, 2006], is drawn on all figures.

[16] Resolution modeling with independent checkerboard tests for Vp and Vs are presented in Figure A1. In these tests, the calculated synthetic absolute and differential travel-times are included only for the same data distribution as for the real data. Following the standard procedure, we add uniformly distributed random noise to the synthetic data in the interval ±0.025 s for P waves and ±0.05 s for S waves. The inverted models are obtained with the same inversion scheme as the real data set and starting from the same 1D model. The synthetic input P- and S-wave velocity models consist of 6 × 6 × 6 km patches with velocities alternatively +5% and −5% compared to the normal starting model (Top figures, Figure A1). Recovered P and S wave models are presented underneath. It is clear that features are well recovered in the center of the two upper layers. At 12 km depth, we observe some smearing of the recovered patche, due to the much smaller density of rays.

4. Tomography Results

[17] The results of the tomography are presented in the three figures. Relocated hypocenters are shown scaled by magnitude on map view (Figures 2b), along a longitudinal cross-section following the fault direction (N57°E strike) (Figure 3I), and along four cross-sections perpendicular to the fault (Figure 3II). Figure 3III compares cross-sections through the highest density aftershock region (segment B) with overlying topographic and bathymetric profiles. The P and S velocities are presented in Figure 4.

4.1. Hypocenter Location

[18] The aftershock sequence can be broken into four distinct segments based on the event density and spatial relations relative to the main shock (Figures 2b and 3). Southwest of the main shock, the activity between 3°20′E and 3°40′E forms a denser cloud of seismicity than activity to the NE. The maximum depth of aftershocks increases from 15 km in the southwest to 22 km in the northeast (Figure 3). We refer to the segments as A, B, C, and D throughout the remaining discussion, with A occurring furthest SW and D occurring furthest NE.

[19] Segment A can be subdivided into three clusters (Figures 3I and 3II, A). The southernmost cluster (Figure 2b at $X = 0$ km, $Y = 0$ km, pale-gray hypocenters on Figure 3 II, A), at the easternmost edge of the Mitidja basin, includes the 29 May Md = 5.8 aftershock [*Bounif et al.*, 2004]. The hypocenters are aligned between 6 and 14 km depth on an apparent plane dipping about 75°SE. When viewed in cross-section along a N10°E direction, perpendicular to the E–W oriented fault plane of the large aftershock, the dip of the fault plane is 70°S. The northernmost cluster, which is about 10 km long, follows the coast line and is oriented ∼N100°E. These aftershocks are located in the area of the 28 May Md = 5.0 aftershock, and this cluster seems to follow the trace of the Thenia fault (TF, Figure 1b). When viewed perpendicular to strike, these events exhibit near vertical alignment (Figure 3 II A). A third cluster of events is observed in between the previous two clusters and extends from 5 to 13 km depth with a near vertical geometry (Figure 3 II A). We interpret these as occurring on the western end of the main shock fault.

[20] The largest segment (Figure 3 I B) is located to the south west of the mainshock location around the Zemmouri village and in the area of the 27 May (Md = 5.8) major aftershock. This segment is characterized by the concentration of a large number of aftershocks striking NNW–SSE. The cross section through this segment suggests an approximately 40°SE dipping trend visible below 5 km depth down to 12–15 km (Figure 3 II B). This plane may correspond to the primary thrust fault. We interpret the scatter to indicate that most of the aftershocks lie in the footwall block, which is commonly observed for thrust faults events. This scenario is also comparable to the El Asnam central fault segment [*Yielding et al.*, 1989]. More

Figure 3. Vertical cross sections through the relocated aftershocks. At the top (I): cross section along strike (Y line) in the azimuth N57°E. The white star shows the mainshock location. The four segments identified by seismicity density and discussed in the text are also shown (A, B, C, and D). Left (II): four segments shown in cross sections taken perpendicular to the main shock fault strike. The azimuth of cross sections is N327°E through the four segments, except through the northernmost part of A segment (on the right of the black dashed line), where it is N10°E. Pale-gray aftershocks belong to the southernmost cluster of A segment. Scale 1/1. Right (III): four vertical cross sections through the B segment, along the lines X = 12 km to X = 21 km (azimuth N327°E). The width of each section is 3 km. The upper parts show the topographic and bathymetric profiles.

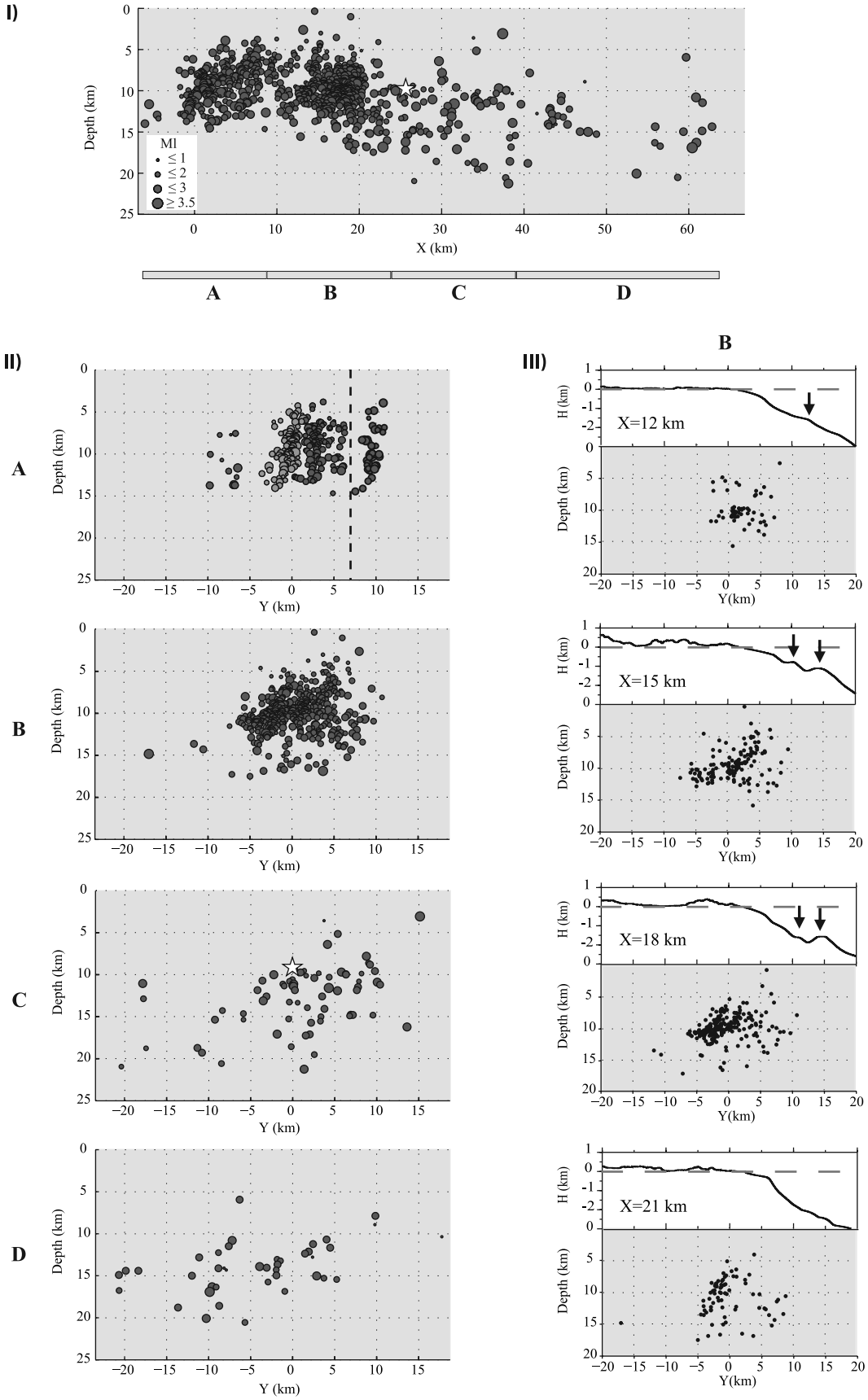
I)
Depth (km)
X (km)
Ml
≤ 1
≤ 2
≤ 3
≥ 3.5
A
B
C
D
II)
III)
B
Y (km)
H (km)
Y(km)
X=12 km
X=15 km
X=18 km
X=21 km

Figure 3

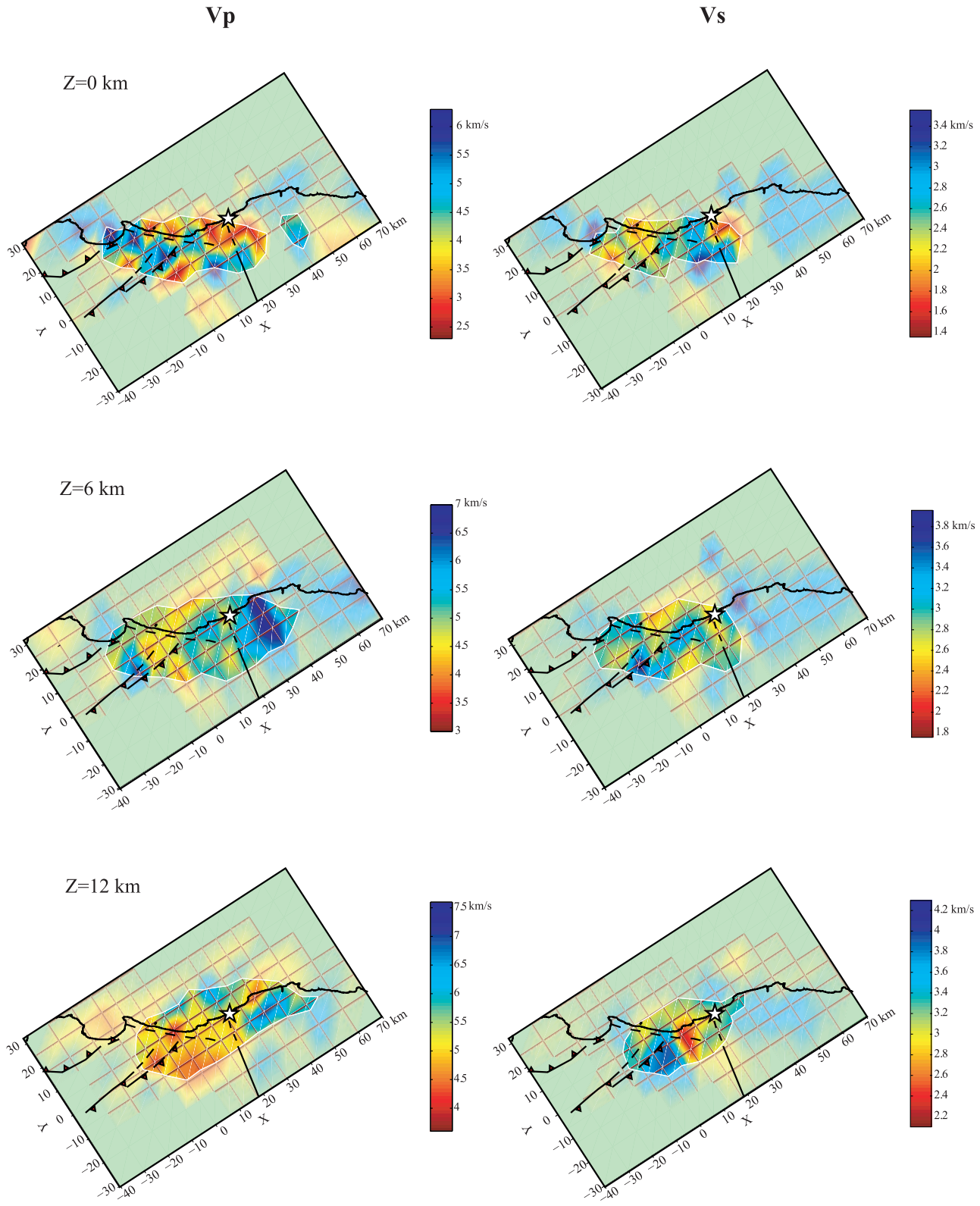

Figure 4. Map view of the P- and S-wave velocity models at different depth levels. The colorbars are centered on the initial velocity in the layer. Unresolved parts, where DWS is lower than 25, are made opaque. A schematic frame is superimposed, showing the coast line, main shock, and the major tectonic structures.

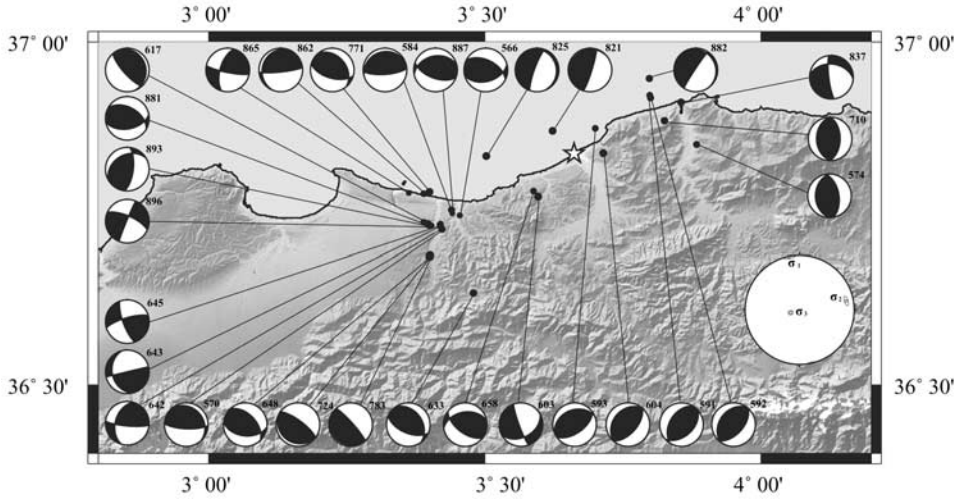

Figure 5. Fault mechanisms of 30 aftershocks, compatible with the deduced stress tensor presented in the inset.

detailed cross sections (Figure 3 III, X = 12 to 21 km), reveal a more complex image of the rupture zone. On profile X = 12 km, a little scarp can be observed on the sea floor at Y = 12 km (see the arrows in Figure 3 III) and may coincide with the surface extension of the 40°–45°SE dipping seismicity. Along X = 15 km and X = 18 km, two scarps are observed on the topographic profile and appear to coincide with the surface extension of two parallel seismic clusters and likely related fault planes dipping again 40°–45°SE. The inferred dip of the seismicity clusters is comparable to the 44°SE dipping Harvard-CMT fault plane solution. The scarp morphology is not clearly observed on the profile X = 21 km, although the SE dipping fault plane is defined by the seismicity. It is important to note that in all cross sections, the extension of aftershocks toward the surface reaches the seafloor at a maximum of 8 to 10 km from the shoreline in the epicentral zone of the M_w = 6.8 earthquake.

[21] Segments C and D are located NE of the main shock (Figures 2 and 3). In this easternmost part, the aftershock distribution becomes more scattered and extends deeper. The sparseness of activity is a real feature of the aftershock sequence and is not due to data selection for tomography (Figures 2a and 2b). The deepest hypocenters are located ashore, where depths are well controlled by local seismic stations. However it is clear that some shallow small magnitude earthquakes may have been eliminated during the initial localization stage. In the C segment there is a possible ~45°SE dipping alignment to the seismicity. The 8 to 10 km depth for the main shock is consistent with the fault plane defined by the aftershocks on the C segment, with the aftershocks lying in the footwall block.

4.2. Velocity

[22] Six tomographic images are displayed in Figure 4 showing the P- and S-wave velocity models obtained by tomoDD at depth levels 0, 6 and 12 km. For each layer, the velocity scale is centered on the initial velocity used in the inversion process for this specific layer. Unresolved parts, where DWS are lower than 25, are made opaque.

[23] At the surface, high P-wave velocities are observed under Cap Matifou where the basement outcrops (Figure 1b). A low velocity strip is observed along the western border of the Mitidja basin. Neogene units and overlying marine terraces around Zemmouri (Figure 1b) are marked by low velocities. The S-wave velocities are low in the Mitidja Quaternary basin and higher in the Tell Atlas (basement rocks).

[24] At 6 km depth, a high P velocity zone is observed in the eastern part of the images, where the basement is present. The eastern termination of the Mitidja basin is underlined by lower P velocity and higher S velocity. The simplest image corresponds to the 12 km depth layer, where a high P velocity zone to the east juxtaposes a large low velocity region to the west. This region corresponds to low S velocity around Boumerdes and high velocity west of the Blida thrust system (Figure 1a).

5. Focal Mechanisms and Regional Stress Tensor

[25] Following *Rivera and Cisternas* [1990], we determined the best fitting stress tensor based on inversion of P-waves polarities, azimuths to the stations and the take-off angles. We selected events with at least 9 polarities and used 57 reliable aftershocks, whose focal mechanism can be constructed with no more than one wrong polarity. This result in nearly 600 polarities and related parameters for use in the stress tensor inversion.

[26] The fault plane solutions of 30 aftershocks presented in Figure 5, computed following *Rivera and Cisternas* [1990] method, were constructed without any inconsistent polarities. The parameters defining the nodal planes, azimuth, dip and rake according to Aki's convention [*Aki and Richards*, 1980] are presented in Table 1 for the full set. The complete focal mechanisms, including polarities, are presented in Figure B1.

[27] The majority of the solutions are reverse mechanisms, resembling the main shock and two of the three largest aftershocks. This is particularly true in the epicentral zone and the eastern side of the aftershock cloud. At the eastern extremity of the seismic cloud, some events show

Table 1. The Fault Plane Solutions of the 30 Aftershocks Presented on the Figure 5, Computed Following *Rivera and Cisternas* [1990] Method[a]

Event Number	Date	Time (UT)	Latitude (°)	Longitude (°)	Depth (km)	Ml	Strike (°)	Dip (°)	Rake (°)
566	2003/06/01	06:44	36.764	3.460	8.9	2.5	297	53	119
570	2003/06/01	09:00	36.742	3.428	7.5	2.9	318	22	133
574	2003/06/01	12:02	36.886	3.839	13.2	2.8	350	55	84
584	2003/06/02	00:06	36.761	3.444	7.9	2.3	86	73	94
591	2003/06/02	04:21	36.897	3.779	15.7	2.7	212	45	79
592	2003/06/02	04:42	36.894	3.780	15.7	2.8	217	35	86
593	2003/06/02	05:01	36.861	3.680	17.0	2.7	246	33	100
603	2003/06/02	17:21	36.767	3.593	10.1	3.1	160	83	−131
604	2003/06/02	22:30	36.848	3.712	16.8	3.1	220	32	89
617	2003/06/03	18:48	36.753	3.399	9.2	2.7	341	16	112
633	2003/06/04	17:18	36.647	3.488	11.4	3.0	325	36	117
642	2003/06/05	05:17	36.739	3.430	7.5	2.9	95	80	134
643	2003/06/05	11:32	36.743	3.429	10.1	2.8	257	90	59
645	2003/06/05	14:06	36.746	3.430	9.9	2.6	160	74	165
648	2003/06/05	21:54	36.706	3.411	11.7	2.0	317	51	118
658	2003/06/07	18:44	36.792	3.583	11.6	2.7	127	59	119
710	2003/06/10	19:12	36.890	3.797	15.0	3.0	179	38	88
724	2003/06/12	01:02	36.708	3.410	10.9	3.4	121	16	85
771	2003/06/16	21:51	36.797	3.405	9.8	3.1	321	36	119
783	2003/06/18	00:58	36.708	3.411	10.6	3.2	126	8	78
821	2003/06/21	04:17	36.852	3.609	11.6	3.1	233	8	125
825	2003/06/21	11:01	36.819	3.508	12.9	3.1	340	13	−129
837	2003/06/22	17:17	36.902	3.826	15.4	3.0	173	80	−52
862	2003/06/24	02:34	36.795	3.394	10.6	2.7	84	82	105
865	2003/06/24	17:44	36.807	3.365	9.5	2.4	101	80	151
881	2003/06/26	13:03	36.747	3.407	10.0	3.1	299	48	119
882	2003/06/26	13:57	36.933	3.778	14.0	2.9	323	10	−160
887	2003/06/27	02:12	36.768	3.443	8.6	2.8	110	59	109
893	2003/06/27	15:55	36.746	3.407	9.5	2.6	7	67	63
896	2003/06/27	23:43	36.745	3.408	9.5	2.7	203	87	−20

[a]For the full set, we give the date and time, the coordinates of the hypocenter, the magnitude, and the parameters defining the nodal planes, azimuth, dip and rake according to Aki's convention [*Aki and Richards*, 1980].

reverse faulting on planes striking about NS. Some strike-slip and normal faulting solutions are however found especially at the westernmost end of the aftershocks cloud. Perhaps these events occurred on pre-existing faults reactivated by the major event.

[28] The stress tensor is inset in Figure 5. The shape factor R, represents the ratio between (σ_z-σ_x) and (σ_y-σ_x). R < 0 corresponds to a reverse stress regime with ($\sigma_z = \sigma_3$), R > 1 corresponds to a normal faulting stress field with ($\sigma_z = \sigma_1$), and 0 < R < 1 represents a strike-slip regime with ($\sigma_z = \sigma_2$). For the Zemmouri region, R = −1.5 indicating a reverse stress regime. The stress tensor obtained has a nearly horizontal N350°E maximum principal stress (σ_1) direction, a nearly vertical minimum principal stress (σ_3) direction and a nearly horizontal N80°E intermediate principal stress (σ_2) direction. This finding is consistent with the stress tensor obtained from the inversion of focal mechanisms along the plate boundary [*Stich et al.*, 2003] (see Figure 1a, inset). In northern Algeria NE–SW trending reverse and thrust faulting is the predominant feature present along the Tell Atlas, controlling the morphology of the Mitidja and Chelif Quaternary basins (Figures 1a and 1b) [*Meghraoui*, 1988]. The stress tensor obtained from the Zemmouri earthquake sequence is similar to that obtained by inversion for the Chenoua-Tipasa earthquake of October 29th 1990, M = 6.0, [*Bounif et al.*, 2004] with local data. The principal stress direction differs by 12° from the median P-axis orientation (N338°E) of thrust and strike-slip events found by *Braunmillller and Bernardi* [2005] with regional data.

6. Discussion and Conclusion

6.1. Fault Geometry

[29] The spatial distribution of relocated aftershocks allows us to differentiate four seismic segments on the main fault and two clusters occurring on secondary faults (Figure 3). Seismicity along segment A, at the western end of the aftershocks cloud, exhibits a nearly vertical geometry between 4 and 14 km. Seismicity along segment B, between Boumerdes and the main shock location, occurs from the surface to 18 km, with most activity focused between 5 and 13 km depth. These aftershocks likely enclose a 40 to 50°SE dipping en echelon fault system with strands separated by 3 km (Figure 3 III). The activity abruptly decreases east of the main shock however up to Cap Djinet (C segment), where a 45°SE dipping plane can be seen between 3 and 23 km depth. The last segment D is poorly constrained because most aftershocks lie offshore. Two clusters are observed on both sides of the main fault in the A segment. The northernmost cluster is aligned along the Cap Matifou coast, while the southernmost cluster is more concentrated south of the main shock fault. Both display nearly vertical planes from 5–6 to 14 km depth (Figure 3 II A).

[30] Following the Harvard CMT solution, we have taken a value of N57°E for the strike of the fault responsible of the Zemmouri major earthquake. This azimuth is in good

Table 2. Synthesis of Main Shock Parameters[a]

Source	Lat (°)	Long (°)	Depth (km)	Strike (°)	Dip (°)	Rake (°)	Mo (10^{19}Nm)
Harvard-CMT	36.93	3.58	9	57	44	71	2.01
USGS	36.89	3.78	9	54	47	88	1.30
Yagi (2003)	36.83*	3.65*	–	54	47	86	2.40
Delouis et al. [2004]	36.83*	3.65*	–	70	40	95	2.90
Meghraoui et al. [2004]	36.83*	3.65*	–	54	50	88	2.80
Braunmiller and Bernardi [2005]	36.83*	3.65*	18	62	25	82	
(Belabbes et al., submitted manuscript, 2008)	36.83*	3.65*	–	57	45	89	2.16

[a]The epicentral coordinates with * are taken from *Bounif et al.* [2004]. Yagi's model available at: //iisee.kenken.go.jp/staff/yagi/eq/algeria20030521/algeria2003521.html.

agreement with the ~60° orientation of the envelope of the aftershock cloud. Except for *Delouis et al.* [2004] who advocate a N70°E strike from their waveform modeling, other authors have used strikes of around 55° as fixed parameters for their modeling (Table 2).

[31] In the central part of the aftershocks distribution, where the activity is the strongest (B segment in Figure 3 II, X = 15–21 km on Figure 3 III), the dip of the aftershock cloud is well defined at 40° to 50°SE. These values are comparable to the 40° to 47° found for all models of the mainshock, except for *Braunmiller and Bernardi* [2005] who obtained a 25°SE dipping fault (Table 2). The fault complexity is obvious on cross-section X = 18 km, where two dipping parallel clusters that coincide spatially with two scarps are observed on the bathymetric profile. We observe that the NW cluster is most active on X = 15 km profile, while only the SE cluster is active on X = 21 km profile. Since the Zemmouri earthquake occurred on the northeastern continuation of the en-echelon fault system bordering the Mitidja basin to the south (Figure 1b), it would not be surprising to observe the same en-echelon fault system offshore. A comparable surface faulting geometry is observed for the nearby 1980 El Asnam earthquake [*Meghraoui and Doumaz*, 1996]. Whatever the dip taken between 40° and 50°, the fault geometry and related seismicity reaches the seafloor at a distance less than 10 km from the shoreline in the epicentral zone. A comparable result is obtained from the inversion of InSAR data and surface displacement field, which is best fit by a N57° striking fault dipping 45° and reaching the seafloor at 8 km from the shore line (S. Belabbes et al., Rupture parameters of the 21 May 2003, M_w 6.8, Zemmouri (Northern Algeria) earthquake deduced from InSAR, submitted to *Journal of Geophysical Research*, 2008).

[32] *Deverchere et al.* [2004] draw a flat-ramp fault connecting the rupture plane at 7 km depth to the faults scarps that they map 15 to 25 km offshore and which they consider as associated to the earthquake rupture. However this interpretation is not supported by the coastal uplift distribution [*Meghraoui et al.*, 2004] and surface deformation revealed by the InSAR analysis (Belabbes et al., submitted manuscript, 2008). In addition, aftershocks located above 7 km on segments B and C of Figure 3 do not show any change in the fault dip when compared with the deeper seismic events, as would be expected in a ramp-flat system. The interpretation of *Deverchere et al.* [2004] is also inconsistent with the GPS data inversion of *Semmane et al.* [2005] or the regional moment tensor analysis of *Braunmiller and Bernardi* [2005].

[33] The total length of the aftershock cloud observed two months after the main shock is 65 km, but, ten days after the main shock it was only 50 km [*Bounif et al.*, 2004]. The 15 km extension of the seismicity corresponds to a NE migration. In contrast, the strike and depth distribution of the aftershocks did not change with time. Our aftershock relocations by tomoDD in a 3D velocity model differ slightly from those obtained previously by hypoDD [*Bounif et al.*, 2004]. The clearest difference is observed on the location of the northwesternmost aftershocks (between Cap Matifou and Boumerdes) which are now clearly aligned, strengthening the hypothesis of a fault branch parallel to the Thenia fault (Figure 1b). This alignment is consistent with the ~N100°E trending rupture inferred from the INSAR data where the related surface displacement suggests 0.15 m right-lateral slip at depth (Belabbes et al., submitted manuscript, 2008).

[34] The maximum depth of seismicity increases along strike from 15 km to the southwest to 23 km in the northeast, which is different from the previous location of 12 km to 18 km in *Bounif et al.* [2004]. Although the upper 5 km do not show significant seismicity, the minimum depth of hypocenters is problematic particularly for the D segment where seismic events are too far offshore and therefore difficult to record and localize. Since the lack of seismicity in the upper 10 km to the NE could correspond to an area of a future large event, data from OBS would have been useful to constrain hypocenter depths. Alternatively, the lack of seismicity could be due to the fact that the shallow part of the fault slipped during the main rupture, as proposed by *Delouis et al.* [2004].

6.2. Imaging the Fault Zone From Velocity Structures

[35] In spite of the high tectonic complexity of the Boumerdes region, some correlations may be highlighted between geological units and velocity structures. Basement outcrops in the Cap Matifou region are related to higher P velocities in the upper crust. At the same depths, lower velocities correspond to Quaternary filling of the Mitidja Basin and to marine terraces (Figure 1b).

[36] The 12 km depth layer of tomographic images (Figure 4) presents the simplest pattern, with a bimodal distribution of P velocities: a well marked low velocity zone (Vp = 4.5 to 5 km/s) to the west, a normal to slightly higher velocity zone (Vp = 6 to 6.8 km/s) to the east. The transition between these two velocity structures is clearly seen along strike on the Y = 0 km Vp and Vs cross sections (Figure 6). We have to note here that the seismicity is primarily taking place on a dipping plane, so that the vertical velocity profile

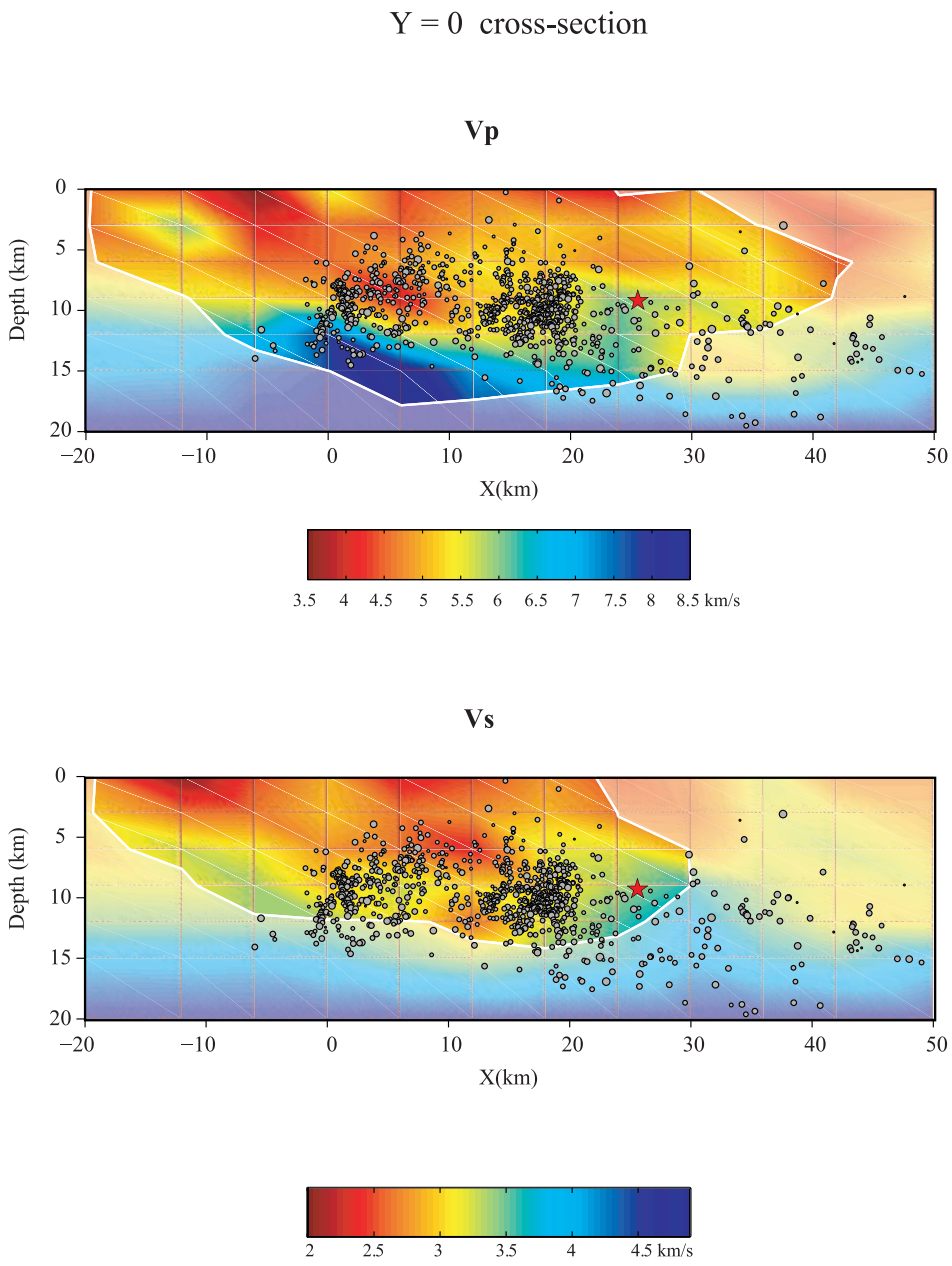

Figure 6. Vertical cross sections through the 3D P- and S-wave velocity models and the complete aftershocks cloud, along strike (Y line), azimuth N57°E. Red star: main shock.

shown in Figure 6 is not a true representation of velocity along the fault itself. This transition is located at the limit between B and C fault segments of Figure 3 I, and precisely at the transition between high level and low level of aftershocks activity. It is also located at the downward projection of the contact between the Blida thrust and fold system and the metamorphic Kabyle Block (KF, Figure 1b, Figure 4). One may also note that the main shock commonly accepted depth at 8 to 10 km, is apparently in the higher velocity block.

[37] Our results show that the velocity model as well as the aftershocks activity differ along the fault zone on both sides of the Zemmouri main shock. Two fault segments were previously identified based on the aftershocks distribution [*Bounif et al*, 2004], by modeling of coastal uplift [*Meghraoui et al.*, 2004], by joint inversion of seismological waveforms and ground displacement observations [*Delouis et al.*, 2004], and by inversion of INSAR data (Belabbes et al., submitted manuscript, 2008). The characteristics of these two slip segments differ in detail depending on study methodology. Along the western slip patch between Boumerdes and Zemmouri, corresponding to the region where a well constrained coastal uplift of 0.75 m has been observed, results from all studies are consistent and comparable. Here, maximum slip, up to 3 m, is concentrated between 2 and 11 km. The eastern patch located between Zemmouri and Dellys, and where a 0.40 m coastal uplift has been observed, is more poorly resolved. It corresponds to a 3 m slip patch below 16 km for *Semmane et al.* [2005], a shallow 1.5 m slip patch for *Delouis et al.* [2004], or a 1.5 m, 12 km depth, slip patch for (Belabbes

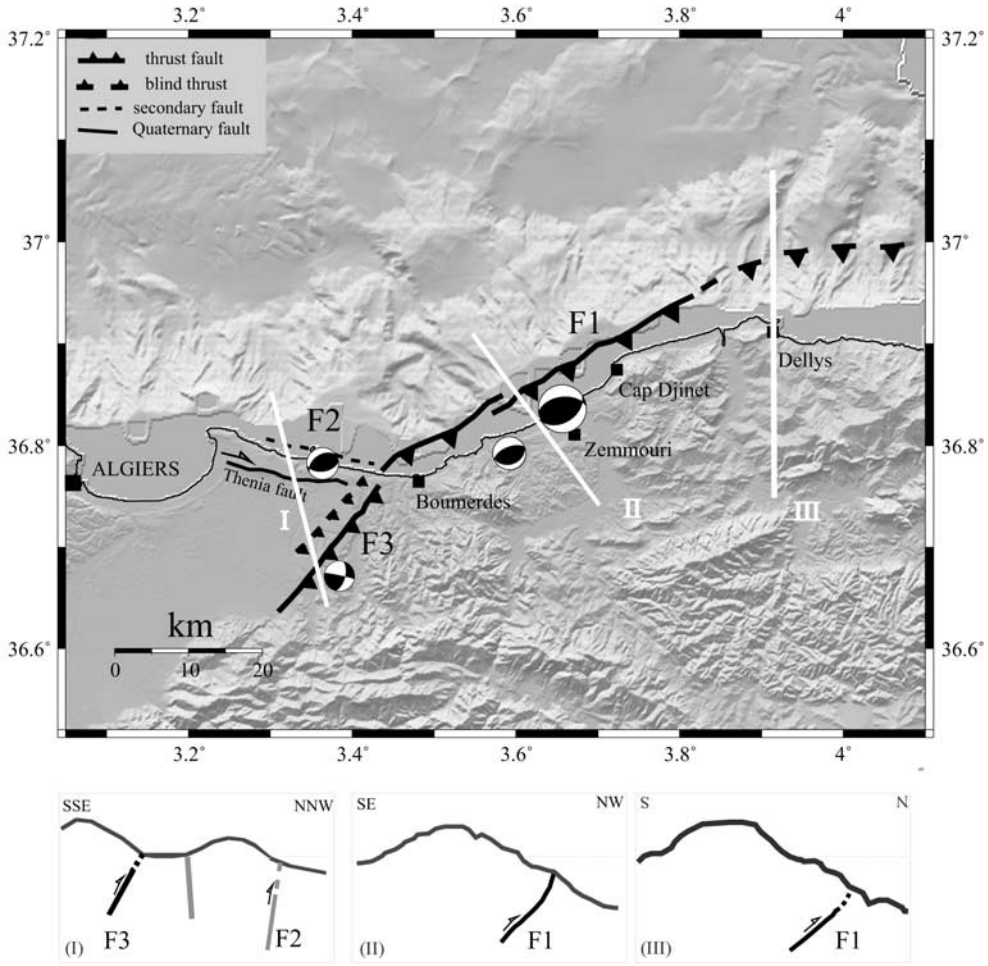

Figure 7. Tectonic model proposed for the 21 May 2003 earthquake rupture and related aftershocks sequence. F1, F2, F3 are represented on the schematic cross sections with their respective geometric and kinematic characteristics.

et al., submitted manuscript, 2008). It is interesting to note that the low velocity zones observed on Vp and Vs profiles (Figure 6), even if they are not drawn along fault dip, correspond to the maximum slip zones of *Delouis et al.* [2004] final model. This observation leads us to suggest that the presence of asperities on the fault is probably related to the geologic structure as well.

[38] In the El Asnam case study, aftershocks concentrated at the edge of a high velocity basement and on the footwall block bordering this unit [*Ouyed et al.*, 1981; *Yielding et al.*, 1989]. On the basis of velocity structures across the El Asnam earthquake area, *Chiarabba et al.* [1997] conclude that fault segmentation and geometrical discontinuities observed along strike are controlled by pre-existing structures imaged by tomography. For the Zemmouri source zone, velocity structure along the fault below 5 km seems to control the seismic activity, but in contrast to what is generally observed, the zones of higher activity and the maximum slip [*Delouis et al.*, 2004] correlate with the lower velocities. Comparable observations by *Kato et al.* [2005] on the 2004 Mid-Niigata prefecture reverse fault type earthquake however show the largest aftershocks and most activity in a slightly low Vp zone, as do we.

[39] In conclusion, the high resolution study of aftershocks and velocity structure associated with the Zemmouri 2003 earthquake allowed us to better constrain the fault geometry and structure in this section of the Tell Atlas (Figure 7). We observe that the thrust fault is related to a complex pattern of seismic activity with variable aftershock density along strike that defines four main segments. The main fault zone F1 strikes about 60°E with en echelon right-stepping and ~45°SE dipping plane. However the southwest end displays three nearly vertical clusters that may correspond to three fault branches, F2 parallel to the Thenia fault, F3 bordering the Mitidja basin and the western end of the main fault in between (Figure 7). The constraint of the Zemmouri aftershocks distribution and earthquake fault rupture geometry provides a basis for the study of nearby fault segments and seismic hazard assessment of the Algiers region.

Appendix A

[40] Figure A1.

Appendix B

[41] Figure B1.

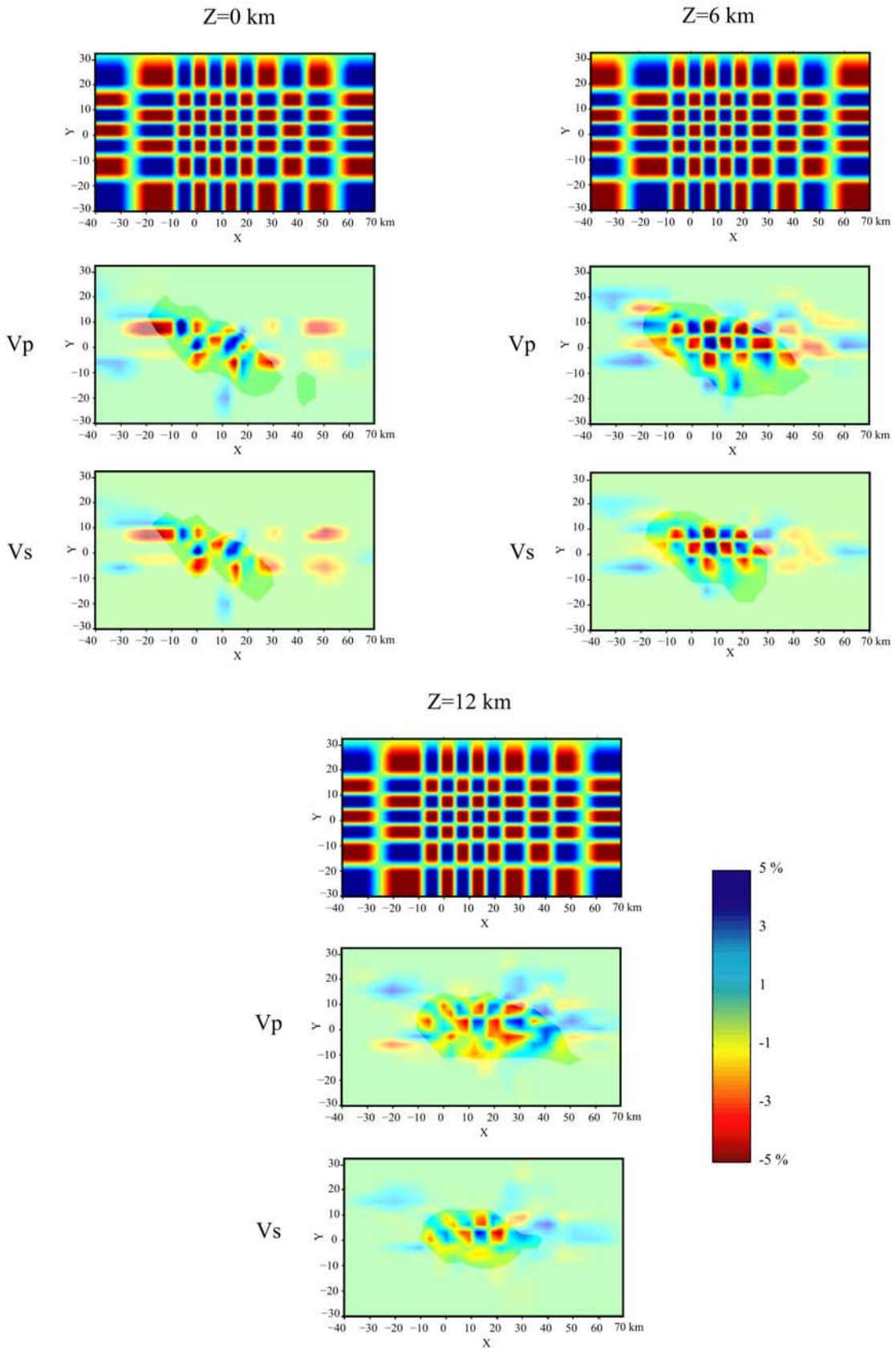

Figure A1. Checkerboard test presented at 3 depths. Top: input perturbation model, consisting of patches of 6 km^3 with velocities ±5% compared to the normal starting model. Bottom: recovered perturbation models for P- and S-waves.

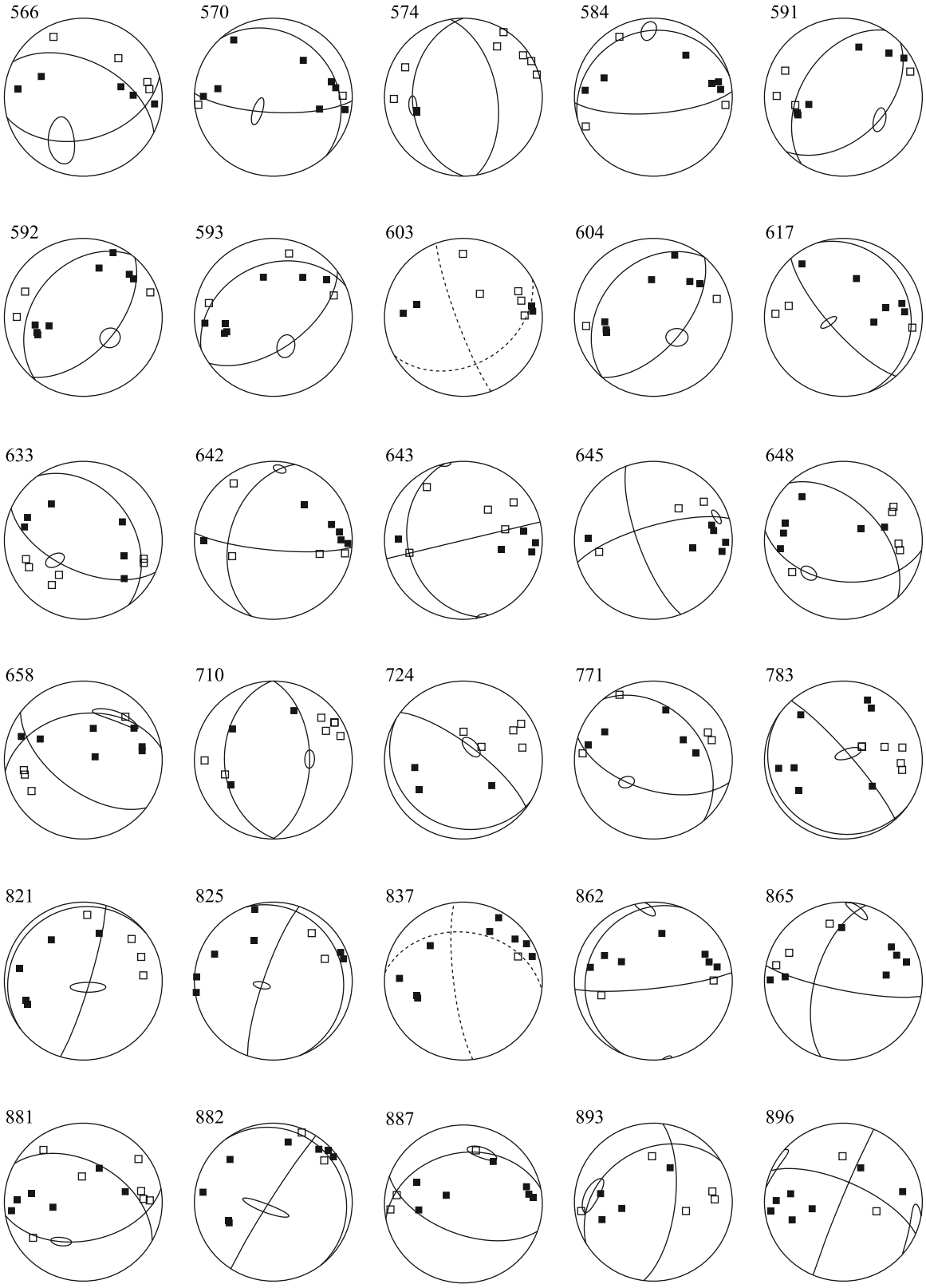

Figure B1. Focal mechanisms obtained by inversion for the 30 events presented in Figure 5, represented on the lower hemisphere equal area projection. Input polarities (black squares are compression), calculated nodal planes, together with one standard deviation ellipse of the pole of one plane when calculated.

[42] **Acknowledgments.** We are grateful to the local authorities in Algeria and Centre de Recherche en Astronomie Astrophysique et Géophysique for the logistical support during the field investigations. We thank Ross Stein for detailed and constructive comments that substantially improved this manuscript, as well as an anonymous reviewer for his/her helpful suggestions and extensive improvement of the text. We thank Samir Belabbes and Cakir Ziyadin (ITU, Turkey) for their assistance in preparing figures and Jacques Deverchere (Brest University) for providing the detailed bathymetry of the earthquake area. Some of the figures were prepared using the public domain GMT software [*Wessel and Smith*, 1998]. This work was supported by the INSU research project ACI Cat-Nat "Risque sismique de la région d'Alger".

References

Aki, K., and P. G. Richards (1980), Quantitative seismology: Theory and methods, W.H. Freeman & Co., San Fransisco, vol. 1, pp. 557.

Argus, D. F., R. G. Gordon, C. Demets, and S. Stein (1989), Closure of the Africa–Eurasia–North America plate motion circuit and tectonics of the Gloria fault, *J. Geophys. Res.*, *94*(B5), 5585–5602.

Ayadi, A., S. Maouche, A. Harbi, and M. Meghraoui (2003), Strong Algerian earthquake strikes near capital city, *Eos Trans. AGU*, *84*(50), 561–568.

Bannister, S., C. Thurber, and J. Louie (2006), Detailed fault structure highlighted by finely relocated aftershocks Arthur's Pass, New Zealand, *Geophys. Res. Lett.*, *33*, L18315, doi:10.1029/2006GL027462.

Bezzeghoud, M., A. Ayadi, A. Sebaï, and H. Benhallou (1994), Seismogenic zones survey by Algerian Telemetred Seismological Network, Case study of Rouina earthquake of January 19th, 1992, *Phys. Earth Planet Inter.*, *84*, 235–246.

Bounif, A., et al. (2004), The 21 May 2003 Zemmouri (Algeria) earthquake M_w = 6.8: Relocation and aftershocks sequence analysis, *Geophys. Res. Lett.*, *31*, L19606, doi:10.1029/2004GL020586.

Bounif, A., M. Bezzeghoud, L. Dorbath, D. Legrand, A. Deschamps, L. Rivera, and H. Benhallou (2003), Seismic source study of the 1989, October 29, Chenoua (Algeria) earthquake from aftershocks, broad-band and strong motion records, *Ann. Geophys.*, *46*(4), 625–646.

Braunmiller, J., and F. Bernardi (2005), The 2003 Boumerdes, Algeria earthquake: Regional moment tensor analysis, *Geophys. Res. Lett.*, *32*, L06305, doi:10.1029/2004GL022038.

Chiarabba, C., A. Amato, and M. Meghraoui (1997), Tomographic images of the El Asnam fault zone and evolution of the seismogenic thrust-related fold, *J. Geophys. Res.*, *102*(B11), 24,485–24,498.

Delouis, B., M. Valée, M. Meghraoui, E. Calais, S. Maouche, K. Lammali, A. Mahsas, P. Briole, F. Benhamouda, and K. Yelles (2004), Slip distribution of the 2003 Boumerdes–Zemmouri earthquake, Algeria, from teleseismic, GPS, and coastal uplift data, *Geophys. Res. Lett.*, *31*, L18607, doi:10.1029/2004GL020687.

Deverchere, J., et al. (2005), Active thrust faulting offshore Boumerdes, Algeria, and its relations to the 2003 M_w 6.9 earthquake, *Geophys. Res. Lett.*, *32*, L04311, doi:10.1029/2004GL021646.

Frechet, J. (1985), Sismogenèse et doublets sismiques, these d'Etat, Univ. Sci. Et Méd. De Grenoble, France, 206 pp.

Got, J.-L., J. Frechet, and F. W. Klein (1994), Deep fault plane geometry inferred from multiple relative relocation beneath the south flank of Kilauea, *J. Geophys. Res.*, *99*(B8), 15,375–15,386.

Harbi, A., S. Maouche, A. Benouar, D. Panza, and G. F. Benhallou (2004), Seismicity and tectonics structures in the site of Algiers and its surroundings: A step towards microzonation, *Pure Appl. Geophys.*, *161*, 949–967.

Kato, A. E., N. Kurashimo, S. Hirata, T. Sakai, S. Iwasaki, and T. Kanazawa (2005), Imaging the source region of the 2004 mid-Niigata prefecture earthquake and the evolution of a seismogenic thrust-related fold, *Geophys. Res. Lett.*, *32*, L07307, doi:10.1029/2005GL022366.

Klein, F. W. (1978), Hypocentres location programm HYPOINVERS, Open-file Rep. 78–694 (US Geological Survey, Boulder, CO, USA).

Maury, R. C., et al. (2000), Post-collisional Neogene magmatism of the Mediterranean Maghreb margin: A consequence of slab breakoff, *C. R. Acad. Sci. Paris*, *331*, 159–173.

Meghraoui, M. (1988), Géologie des zones sismiques du nord de l'Algérie: tectonique active, paléoséismologie et synthèse sismotectonique. Ph.D. thesis., Univ. Paris-Orsay, Paris, France, 356 pp.

Meghraoui, M. (1991), Blind reverse faulting system associated with the Mont Chenoua Tipasa earthquake of the 29th October 1989 (north-central Algeria), *Terra Nova*, *3*, 84–93.

Meghraoui, M., and F. Doumaz (1996), Earthquake induced flooding and paleoseismicity of the El Asnam (Algeria) fault-related fold, *J. Geophys. Res.*, *101*(B8), 17,617–17,644.

Meghraoui, M., S. Maouche, B. Chemaa, Z. Cakir, A. Aoudia, A. Harbi, P. J. Alasset, A. Ayadi, Y. Bouhadad, and F. Benhamouda (2004), Coastal uplift and thrust faulting associated with the M_w = 6.8 Zemmouri (Algeria) earthquake of 21 May, 2003, *Geophys. Res. Lett.*, *31*, L19605, doi:10.1029/2004GL020466.

Mokrane, A., A. Ait Messaoud, A. Sebai, A. Ayadi, M. Bezzeghoud, and H. Benhallou (1994), Les séismes en Algérie de 1365 à 1992, edited by the Centre de Recherche en Astronomie Astrophysique et Géophysique, Algiers, Algeria, 227 pp.

Nocquet, J. M., and E. Calais (2004), Geodetic measurements of crustal deformation in the Western Mediterranean and Europe, *Pure Appl. Geophys.*, *161*(3), 661–681.

Ouyed, M. (1981), Le tremblement de terre d'El Asnam du 10 Octobre 1980: Etude des répliques, Doctorat de 3ème Cycle, thesis, Univ. De Grenoble, Grenoble, France, 227 pp.

Ouyed, M., M. Meghraoui, A. Cisternas, A. Deschamps, J. Dorel, J. Fréchet, R. Gaulon, D. Hatzfeld, and H. Philip (1981), Seismotectonics of the El Asnam earthquake, *Nature*, *292*, 26–31.

Rivera, L., and A. Cisternas (1990), Stress tensor and fault plane solutions for a population of earthquakes, *Bull. Seismol. Soc. Am.*, *80*, 600–614.

Semmane, F., M. Campillo, and F. Cotton (2005), Fault location and source process of the Boumerdes, Algeria, earthquake inferred from geodetic and strong motion data, *Geophys. Res. Lett.*, *32*, L01305, doi:10.1029/2004GL021268.

Stich, D., C. J. Ammon, and J. Morales (2003), Moment tensor solutions for small and moderate earthquakes in the Ibero-Maghreb region, *J. Geophys. Res.*, *108*(B3), 2148, doi:10.1029/2002JB002057.

Thurber, C. (1983), Earthquake location and three-dimensional crustal structure in the Coyote Lake area, central California, *J. Geophys. Res.*, *88*(B10), 8226–8236.

Waldhauser, F. (2001), hypoDD–A program to compute double-difference hypocenter locations, *U.S. Geol. Surv. Open File Rep.*, *01-113*, 25.

Waldhauser, F., and W. L. Ellsworth (2000), A double difference earthquake location algorithm: Method and application to the northern Hayward fault, California, *Bull. Seismol. Soc. Am.*, *90*, 1353–1368.

Wessel, P., and H. F. Smith (1998), New, improved version of the generic mapping tools released, *Eos Trans. AGU*, *79*, 579.

Wildi, W. (1983), La chaıcirc;ne tello-rifaine (Algérie, Maroc, Tunisie): Structure, stratigraphie et évolution du Trias au Miocène, *Rev. Geol. Dyn. Geogr. Phys.*, *24*, 201–297.

Yielding, G., M. Ouyed, G. C. P. King, and D. Hatzfeld (1989), Active tectonics of the Algerian Atlas mountains—Evidence from aftershocks of the 1980 El Asnam earthquake, *Geophys. J. Int.*, *99*(3), 761–788.

Zhang, H., and C. H. Thurber (2003), Double-difference tomography: the method and its application to the Hayward fault, California, *Bull. Seismol. Soc. Am.*, *93*(5), 1875–1889.

A. Ayadi, S. Maouche, and F. Ousadou, Centre de Recherche en Astronomie Astrophysique et Géophysique, route de l'observatoire, BP 63, Bouzaréah, 16340 Algiers, Algeria.

M. A. Bounif, Université des Sciences et de la Technologie Houari Boumédienne, Institut des Sciences de la Terre, BP 32, El Alia, Bab-Ezzouar, 16111 Algiers, Algeria.

M. Chikh, Centre de Génie Parasismique, Rue Kaddour Rahim, BP 252, Hussein Dey, 16040 Algiers, Algeria.

C. Dorbath, EOST, 5 rue René Descartes, 67000 Strasbourg Cedex, France. (catherine.dorbath@eost.u-strasbg.fr)

M. Meghraoui, UMR 7516, Institut de Physique du Globe, Strasbourg, France.